Signal-to-Noise in Phase Angle Reconstruction: Dynamic Range Extension Using Phase Reference Offsets*

THOMAS E. CONTURO†‚‡‚§ AND GREGORY D. SMITH¶

†*Department of Molecular Physiology and Biophysics and* ¶*Department of Radiology and Radiological Sciences, Vanderbilt University, Nashville, Tennessee 37232; and* ‡*Department of Radiology and Radiological Science, The Johns Hopkins Medical Institutions, Baltimore, Maryland 21205*

The dynamic range of phase-reconstructed magnetic resonance images is compared to that of magnitude-reconstructed images. From analysis of propagation of errors, the phase angle noise is phase-independent and given in radians by $\sigma(|I|)/|I|$, the noise-to-signal ratio of the corresponding magnitude-reconstructed image. As the phase can range from minus π to π, the phase angle dynamic range is 2π times that of the signal magnitude. These results agree with experiment, verifying that the noise in the two receiver channels is uncorrelated. An artifact-free technique is presented for correcting phase spillover, which further extends the phase angle dynamic range. The reconstruction-based reference phase is adjusted on a local basis so that the boundary of phase wraparound is reconstructed near the center of the $[-\pi, \pi]$ interval. For a particular flow study, the phase signal-to-noise was extended over twofold by spillover correction, to a value 15 times that of the magnitude signal-to-noise. © 1990 Academic Press, Inc.

INTRODUCTION

In many instances it may be desirable to obtain an image of the phase information in the complex nuclear magnetic resonance (NMR) signal. For example, flow information can be obtained from either the magnitude (*1–4*) or the phase (*5–8*) of the NMR signal. Similarly, magnetic susceptibility (*9, 10*), static field inhomogeneity (*11–13*), radiofrequency (RF) field inhomogeneity (*14, 15*), chemical shift (*16–18*), and perfusion (*19, 20*) can all be encoded using either the signal magnitude or phase angle. Inversion recovery (*21–23*) and other pulse sequences producing negative intensities (*24–26*) can be used with phase reconstruction of the real component of the NMR signal. To choose the best technique for informational encoding and reconstruction, it is thus necessary to investigate the theoretical and experimental signal-to-noise ratio (S/N) of phase-reconstructed data compared to magnitude data. Since the relation between phase angle and signal magnitude is often arbitrary for different techniques, comparisons are made of the dynamic range of images reconstructed from the same raw data set, where dynamic range is defined as the maximum signal range relative to the minimum detectable signal (i.e., the noise).

---

* Presented at the seventh annual meeting of the Society of Magnetic Resonance in Medicine, San Francisco, CA, August 1988.

§ MSTP Trainee (NIH Grant GM07347). To whom correspondence should be addressed.

The accuracy and dynamic range of phase angle images have been limited by spillover where phases given by $|\phi| > \pi$ are reconstructed into the $[-\pi, \pi]$ interval. Phase spillover is difficult to avoid, unless conservative methods having poor dynamic range are used to produce small phase changes. Some workers have used the rapidity of phase turnover as an indicator of flow velocity (27, 28), but these results are only qualitative since the phase turnover rate depends on the trajectory of flow and other factors. It is thus important to correct this phase spillover to extend the dynamic range of phase images. Faster velocities can be mapped into the $[-\pi, \pi]$ interval using successive data acquisitions (29), or phase can be "unwrapped" by two-dimensional searches for the phase transition (30). However, these unwrapping algorithms are less robust in complicated biological images than in phantoms, can introduce artifacts, and can miscorrect phases in narrow vessels. An artifact-free spillover correction scheme based on multiple reconstructions of the same raw data set is presented.

THEORY

Noise in magnetic resonance (MR) imaging is produced by (31, 32) (1) electrical resistance in the receiver coil, (2) dielectric and inductive losses in the sample, (3) noise in the preamplifier electronics, and, often not considered, (4) RF transmitter noise. These sources produce noise in the in-phase and out-of-phase NMR signals, from which the noise in the magnitude- and phase-reconstructed images can be derived.

The phase angle (ϕ) image is determined from the real and imaginary pixel intensities (I_{re} and I_{im}, respectively) derived from the complex Fourier transform of the signals obtained from the in-phase and out-of-phase receiver channels. The phase angle image is computed pixel-by-pixel according to

$$\phi = \tan^{-1}\left(\frac{I_{im}}{I_{re}}\right). \tag{1}$$

Other methods of reconstructing phase, investigated in NMR spectroscopy (33), are not considered here. Alternatively, the phase angle can be directly detected by using arc–tangent circuitry (34). From the theory of propagation of errors, the standard deviation in phase angle, $\sigma(\phi)$, is given by

$$\sigma^2(\phi) = \left(\frac{\partial\phi}{\partial I_{re}}\right)^2 \sigma^2(I_{re}) + \left(\frac{\partial\phi}{\partial I_{im}}\right)^2 \sigma^2(I_{im}) + 2\rho\left(\frac{\partial\phi}{\partial I_{re}}\right)\left(\frac{\partial\phi}{\partial I_{im}}\right)\sigma(I_{re})\sigma(I_{im}), \tag{2}$$

where ρ is the coefficient for correlation between the real and imaginary noise fluctuations. This expression is valid for arbitrary $\sigma(I_{re})$ and $\sigma(I_{im})$, which are the noise in the real and imaginary images, respectively. The partial derivatives in Eq. [2] can be obtained from Eq. [1] using the chain rule

$$\frac{\partial\phi}{\partial I_{re}} = \frac{\partial\phi}{\partial[\tan(\phi)]} \cdot \frac{\partial[\tan(\phi)]}{\partial I_{re}}, \tag{3}$$

and a similar expression for $\partial\phi/\partial I_{im}$. By taking the tangent of Eq. [1] and differentiating, Eq. [3] becomes

$$\frac{\partial \phi}{\partial I_{re}} = \cos^2\phi \cdot \frac{-I_{im}}{I_{re}^2} . \tag{4}$$

and the analogous imaginary equation

$$\frac{\partial \phi}{\partial I_{im}} = \frac{\cos^2\phi}{I_{re}} , \tag{5}$$

Substituting Eqs. [4] and [5] into Eq. [2],

$$\sigma^2(\phi) = \frac{\cos^4\phi}{I_{re}^2} \sigma^2(I_{im}) + \cos^4\phi \frac{I_{im}^2}{I_{re}^4} \sigma^2(I_{re}) - 2\rho \frac{\cos^4\phi}{I_{re}^3} I_{im}\sigma(I_{re})\sigma(I_{im}). \tag{6}$$

If the noise in the two channels were correlated, stochastic increases in the real signal amplitude would be associated with proportional increases in the imaginary signal amplitude, so that the ratio in Eq. [1] would be unaffected. Thus, correlated noise would contribute to $\sigma(I_{re})$ and $\sigma(I_{im})$ but not to $\sigma(\phi)$. For example, for instantaneous correlated noise in real and imaginary intensities having the same sign, $\rho \geqslant 0$ and the last term in Eq. [6] subtracts from $\sigma(\phi)$. Similarly, for real and imaginary intensities which have opposite signs, $\rho \leqslant 0$ and the last term in Eq. [6] again subtracts from $\sigma(\phi)$ since the last term is odd in I_{re} and I_{im}.

For mathematical simplicity, the noise is assumed to be uncorrelated; i.e., $\rho = 0$ and fluctuations due to the transmitter and receiver coil, dielectric and inductive losses, and preamplifier noise are assumed not to cause proportional fluctuations in the two detected signals. Noise from inductive effects, which is a significant noise source (31), should have a random phase since conductor motions in the sample are random. Thus, inductive effects should produce uncorrelated noise. The preamplifier may introduce correlated noise since the signal is preamplified before phase-sensitive detection is performed (35). The RF transmitter may also contribute correlated noise, as is known to be the case for microwave noise in electron paramagnetic resonance (36), because fluctuations in RF power similarly scale the two channel signals. Agreement of experimental results with theoretical results derived by setting $\rho = 0$ provides an indicator of the absence of correlated noise sources.

The real and imaginary images are also assumed to have equal noise, a valid assumption if the electronics of the two receiver channels have the same noise level and if the same analog-to-digital (A/D) sampling rate and number of samples are used for each channel. The noise in the two channels is also independent of intensity as shown by others (37). Therefore, the noise both in the real and imaginary images will be set to the inherent intensity-independent signal noise, which is referred to as $\sigma(I_0)$. Then, $\sigma(I_{re}) = \sigma(I_{im}) = \sigma(I_0)$ and, with $\rho = 0$, Eq. [6] becomes

$$\sigma^2(\phi) = \sigma^2(I_0)\left(\frac{\cos^4\phi(I_{im}^2 + I_{re}^2)}{I_{re}^4}\right) , \tag{7}$$

or

$$\sigma(\phi) = \sigma(I_0)\left(\frac{\cos^2\phi \cdot |I|}{I_{re}^2}\right) \tag{8}$$

using the definition of the intensity magnitude $|I|$ given by the square root of the sum of the squares of the real and imaginary signal components.

From the definition of ϕ in Eq. [1], $\cos(\phi) = I_{re}/|I|$, so that Eq. [8] becomes

$$\sigma(\phi) = \frac{\sigma(I_0)}{|I|}, \qquad [9]$$

where ϕ is in radians.

The noise of the real and imaginary images can also be compared with the noise in the magnitude-reconstructed image. The magnitude intensity, $|I|$, has a noise given by the propagation of error

$$\sigma^2(|I|) = \left(\frac{\partial|I|}{\partial I_{re}}\right)^2 \sigma^2(I_{re}) + \left(\frac{\partial|I|}{\partial I_{im}}\right)^2 \sigma^2(I_{im}) \qquad [10]$$

$$= \frac{I_{re}^2}{I_{re}^2 + I_{im}^2}\, \sigma^2(I_{re}) + \frac{I_{im}^2}{I_{re}^2 + I_{im}^2}\, \sigma^2(I_{im}), \qquad [11]$$

again assuming the absence of correlated noise. Since $\sigma(I_{re}) = \sigma(I_{im})$, Eq. [11] becomes

$$\sigma(|I|) = \sigma(I_{re}) = \sigma(I_{im}) = \sigma(I_0), \qquad [12]$$

which is valid for signals sufficiently above background noise (37a). For cases of $|I| < 2\sigma(I)$, $\sigma(|I|)$ is then given in terms of $\sigma(I_0)$ (37b) and can be as low as $0.66\sigma(I_0)$ (37a, 37b). Thus, the real and imaginary images usually have the same noise as the modulus image. However, since the real image has twice the available signal range as the modulus image, phase reconstruction of real images in inversion recovery methods (21–23) and other techniques (24–26) truly yields twice the dynamic range as corresponding magnitude-reconstructed images.

Using [12], Eq. [9] can then be written as

$$\sigma(\phi) = \frac{\sigma(|I|)}{|I|}. \qquad [13]$$

Equation [13] states that the noise level of the phase angle image, in radians, is given by the noise-to-signal ratio of the magnitude-reconstructed image. This expression is valid on a pixel-by-pixel basis and for $|I| > 2\sigma(I_0)$. Moreover, since no assumption concerning the phase angle was made, and since the right-hand side of Eq. [13] has no ϕ dependence, the phase angle noise is *independent* of the actual phase angle. Equation [13] contains the assumptions that the noise in the two receiver channels is (a) uncorrelated, (b) equal, and (c) independent of signal intensity (37).

METHODS

Pulse Sequence and Data Acquisition

Magnitude- and phase-reconstructed images were produced using an RF and gradient pulse sequence for flow velocity imaging which was programmed on a Technicare 0.5-T superconducting clinical unit. The orthogonal bipolar gradient sequence (6, 8) contained three interleaved spin-echo sequences and data acquisitions in succession for

each phase-encoding step. The first of these interleaved sequence groups (or subsequences) had no bipolar gradient, the second had a bipolar gradient along x (the frequency-encoding direction), and the third had a bipolar gradient along y (the phase-encoding direction). Only images for the x-bipolar gradient subsequence are presented for illustrative purposes. Partial flow compensation along x was produced by applying the x compensation gradient immediately prior to the x readout gradient. The gradient duration for readout compensation was tuned to minimize shifts in phase in the x direction obtained from stationary samples. The sequence was run with an echo time (TE) of 73 ms, a repetition time (TR) of 500 ms, and 128 phase-encoding steps for each subsequence. Transmitter and receiver coils were linearly polarized and phase-sensitive detection (35, 38) was used. Four signals were averaged in a phase-cycling mode (39) to minimize phase errors, with a net scanning time of 14.8 min to collect all three above subsequences. Readout gradient strength and phase-encoding gradient duration were maximally increased by 60% over standard head coil settings to yield a resolution of 0.625 mm in x (256 pixels) and 1.25 mm in y (128 data points interpolated to 256 pixels with sinc interpolation). The Gaussian $\pi/2$ and π pulses were at the ^1H resonance frequency and RF pulse attenuations were tuned. Twenty initial RF and gradient repetitions were used without readout to minimize phase smear artifacts associated with non-steady-state acquisitions (40). Imaging was with a slice thickness of 50 mm which included the full thickness of the entire phantom, or alternatively a thin slice of 2.5 mm was obtained by doubling the Gaussian pulse widths to 4 ms (π pulse) and 8 ms ($\pi/2$ pulse) and increasing the slice-selecting gradient to a maximum of 0.25 G/cm.

Flow Phantom

Flow was simulated by forcing a 1.5 mM CuSO$_4$ solution through $\frac{3}{8}$-inch-inner-diameter Tygon tubing using a Masterflex pump (Cole-Parmer Co., Chicago, IL) connected to a short segment of Masterflex tubing. This solution was measured to have T_1 and T_2 values of 574 and 319 ms, respectively, using a previously developed method (41). The tube diameter was chosen to simulate the diameter of typical major vessels. The tubing was imaged in air, and a stationary 1.5 mM CuSO$_4$ sample having a thickness equal to the tube diameter was placed inside the frame in the plane of the tube. This provided signal to accurately set the zero- and first-order phase corrections described below.

Image Analysis

Images of both the magnitude (Fig. 1A) and phase (Fig. 1B) of the NMR signal were reconstructed. Phase was reconstructed according to Eq. [1], assigning the phase as either in the $[-\pi, 0]$ interval or the $[0, \pi]$ interval based on the sign of the imaginary pixel intensity. Zero- and first-order phase corrections were made along x during reconstruction for each of the three different subsequences. The phase corrections were interactively set so that the phase of a stationary sample (Fig. 1) was uniformly zero for the one-dimensional Fourier transform of data collected without a phase-encoding gradient. These phase corrections are similar to those used in NMR spectroscopy (42). A constant (zero-order) phase correction was made by linearly combining the sine and cosine transforms of the raw data. A first-order correction varying linearly with
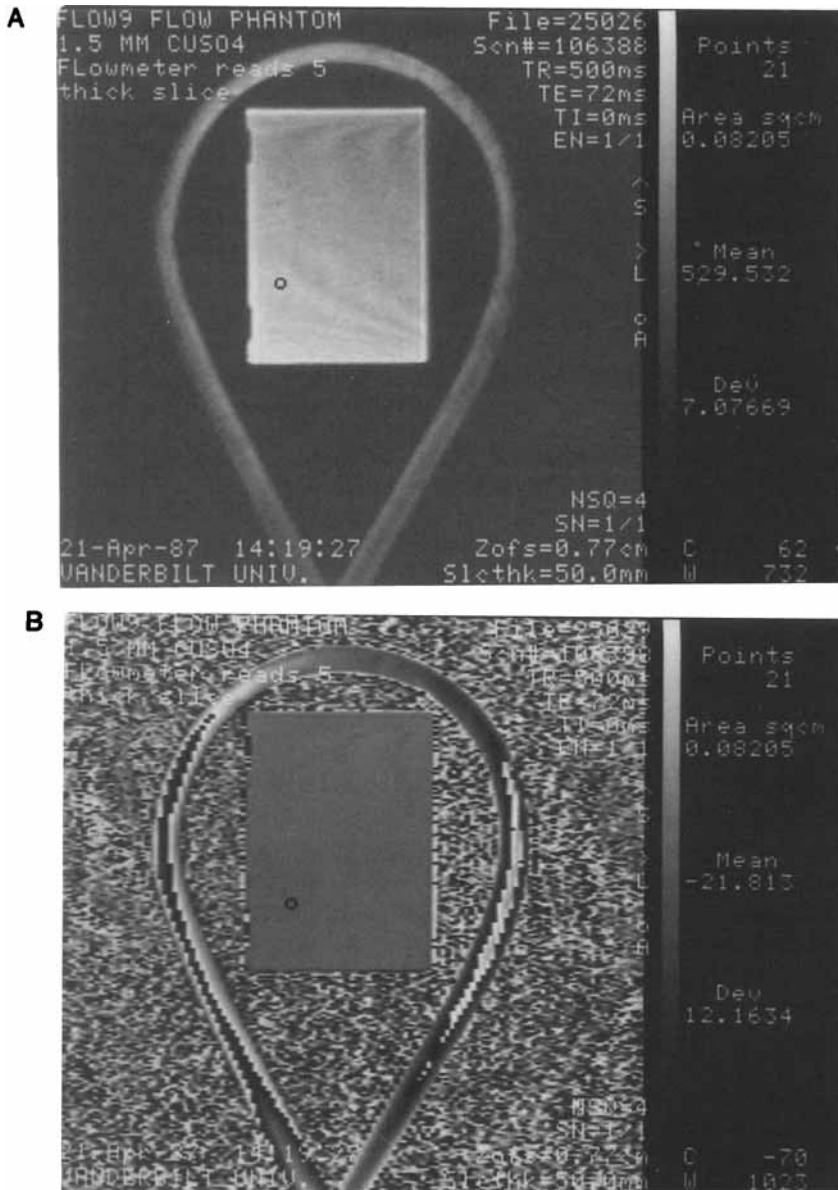
FIG. 1. Magnitude (A) and phase (B) images of a tube containing flowing fluid. Phases greater than π spillover into the negative π region of the $[-\pi, \pi]$ interval. The 21-pixel region of interest was placed in a uniform region to obtain signal-to-noise statistics. A 50-mm slice thickness was used.

Larmor frequency was made by shifting the time origin of all time-domain signals before Fourier transformation. Background phase popcorn noise was eliminated on a pixel-by-pixel basis by setting the pixel phase to zero if the corresponding average pixel intensity magnitude for the three subsequences was below a set threshold. Noise

was measured directly from the standard deviation of an ROI of the phase angle image (Fig. 1). Noise was not determined by the National Electrical Manufacturers Association (NEMA) standard of subtracting two images obtained under the same conditions, since manual phase referencing resulted in baseline phase differences in successively acquired images.

Phase Spillover Correction

Phase spillover was corrected by placing a cursor in the region of spillover and resetting the phase (30) based on $\phi' = 2N\pi + \phi$, where N is the number of "spillovers" in the phase, and where positive N represents wrapping of positive phases into negative phases. Pixel phases were then continuously searched and reset until the spillover boundary was found. As an alternative, a method of spillover correction was developed in which the reconstruction-based reference phase was adjusted for local regions during multiple reconstructions of the raw data (see Results).

RESULTS

Dynamic Range Analysis

The results in Eq. [13] show that the noise of conventionally reconstructed phase angle images is phase-independent, and that the phase dynamic range is a factor of 2π that of corresponding magnitude-reconstructed images. This dynamic range improvement should produce a 2π-fold improvement in signal to noise when tissue and background phases are at opposite limits of the $[-\pi, \pi]$ interval. Experimental signal to noise of the intensity magnitude was measured from the 50-mm slice of the stationary sample in Fig. 1A by dividing the region-of-interest (ROI) mean intensity by the single-pixel standard deviation obtained from the ROI. The ROI was placed in a region of apparent magnitude and phase uniformity. The phase angle noise visually appears to be independent of phase changes around the circular loop (Fig. 1B), in agreement with theory. Thus the experimental phase angle noise was taken from the stationary sample having a zero phase, using the standard deviation of the same ROI. The maximal phase angle signal range is taken as 2π. Experimental results agree with theoretical predictions as summarized in Table 1.

A similar analysis using 2.5-mm slices (Fig. 2) demonstrates better agreement between theory and experiment (Table 1) due to greater uniformity in the magnitude and phase images. The nonuniformity of the thick-slice images is most likely due to static magnetic field inhomogeneity (possibly due to volume averaging of susceptibility difference between air and phantom in the thick-slice case), producing off-resonance effects which would cause both magnitude and phase changes. The artifacts may also be due to through-plane RF phase shifts which are worse in the shorter-duration RF pulses used in the thick slice case. These through-plane RF phase errors produce nonuniformities in both the phase and magnitude (the latter due to volume averaging of phase distributions). The nonuniformity is not likely to be due to spillover of free induction decays (FIDs) into the A/D window which might be caused by imperfect π pulses, since there is no ghosting in the phase-encoding direction and since the slice-selecting z gradient during the π pulse would dephase these FIDs (an infinite projection was not used so that there would be some z-gradient available for dephasing the spurious

TABLE 1

Signal and Noise Measurements of Intensity Magnitude and Phase Angle[a]

Imaged parameter	Signal range	σ	σ/Signal (%)	Dynamic range (relative to $\lvert I \rvert$)
Thick slice[b]				
Signal intensity	529.5	7.1	<u>1.34</u>	75:1
				(1.0)
Phase angle (centiradians)	628.3	<u>1.22</u>	0.19	515:1
				(6.9, or $1.09 \times 2\pi$)
Unwrapped phase angle	1381.3	1.22	0.088	1132:1
				(15.1)
Thin slice[c]				
Signal intensity	3146.4	223.6	<u>7.11</u>	14.1:1
				(1.0)
Phase angle (centiradians)	628.4	<u>7.05</u>	1.12	89.1:1
				(6.3, or $1.006 \times 2\pi$)

[a] Data is taken from Figs. 1 and 2.
[b] 5 cm slice. Numbers which are singly underlined (__) should be equal according to theory.
[c] 2.5 mm slice. Numbers which are doubly underlined (=) should be equal according to theory.

FIDs). The excellent agreement between theory and results in Table 1 also indicates that the noise in the two receiver channels is correctly modeled as uncorrelated in this particular experimental system, and that the assumptions listed in Methods are valid.

Dynamic Range Extension by Phase Spillover Correction

Pixel-by-pixel reassignment of the phase spillover region. For physiologic flows and vessel diameters, significant phase shifts were obtained resulting in large areas of phase spillover, noted in the image in Fig. 1B. The pixels in the region of spillover were searched and assigned a new phase value based on how far the phase has spilled over from the $[-\pi, \pi]$ interval, as described under Methods. The search was based on phase angle sign rather than phase angle gradient since the change in phase across a $-\pi/\pi$ transition is highly dependent on the steepness of true phase in this region. A corrected 2.5-mm-thick phase angle image is in Fig. 3. Artifacts occur at the edge of the spillover region as previously described (*43*). This artifact can be seen in Fig. 3 to cause the pixel on the low-phase side of the spillover region to have an abnormally low phase, and the pixel on the high-phase side of the spillover region to have an abnormally high phase. While these phase errors are also present in the uncorrected phase image (Fig. 2B), the errors are not obvious in the uncorrected image because they are obscured by the phase discontinuity in this region, whereas the errors are conspicuous in the corrected image (Fig. 3) since discontinuities are easily seen in an otherwise continuous image. A similar artifact was found in the 50-mm-thick image in Fig. 1B upon correction (image not shown).
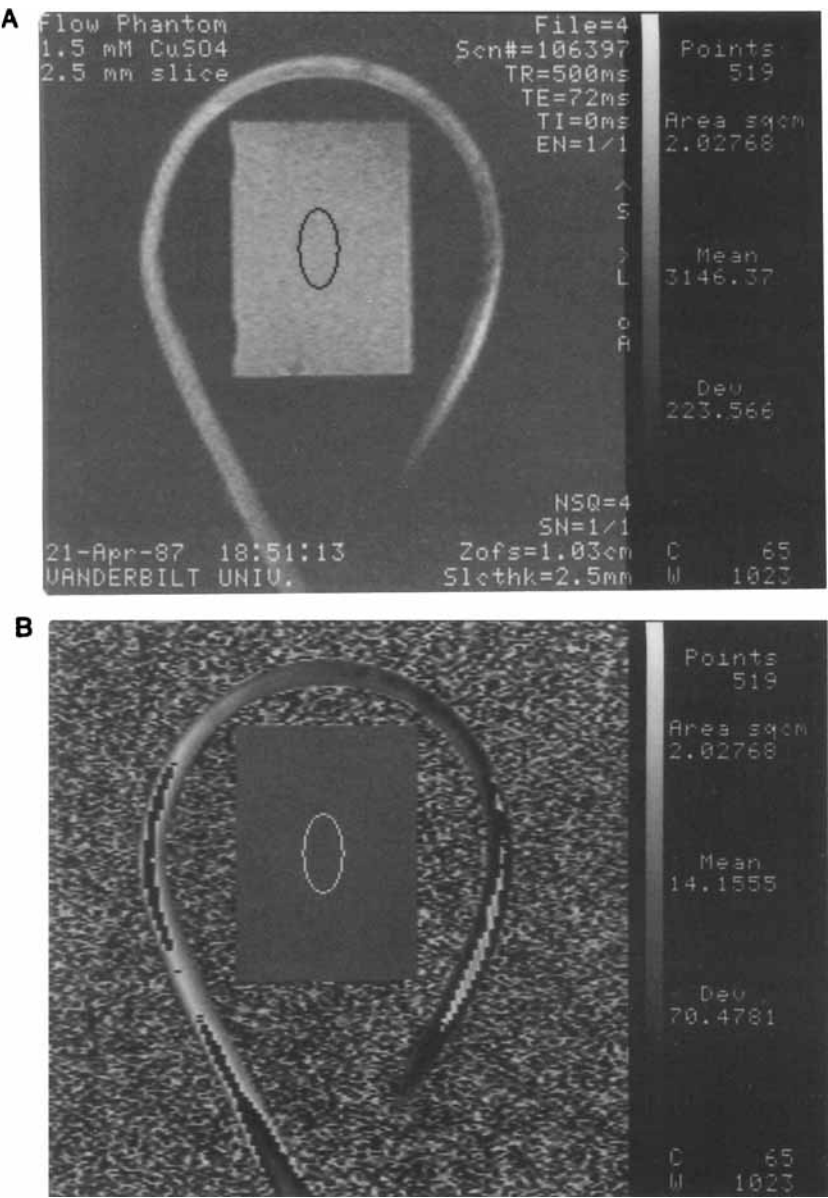
FIG. 2. Magnitude (A) and phase (B) images of the same phantom and same flow rates as in Fig. 1, using a 2.5-mm slice thickness. A larger ROI could be used compared to Fig. 1 because of higher image uniformity.

Phase angle artifacts. The boundary phase artifacts in the corrected images are probably not due to volume averaging of the $-\pi/\pi$ transition since the artifact is similar in the thick-slice and thin-slice images (not shown). The effect of volume averaging can be analyzed by considering the voxel-averaged phase angle tangent, given by $\langle \tan \phi \rangle$ which is the average tangent of ϕ for all the microscopic subelements
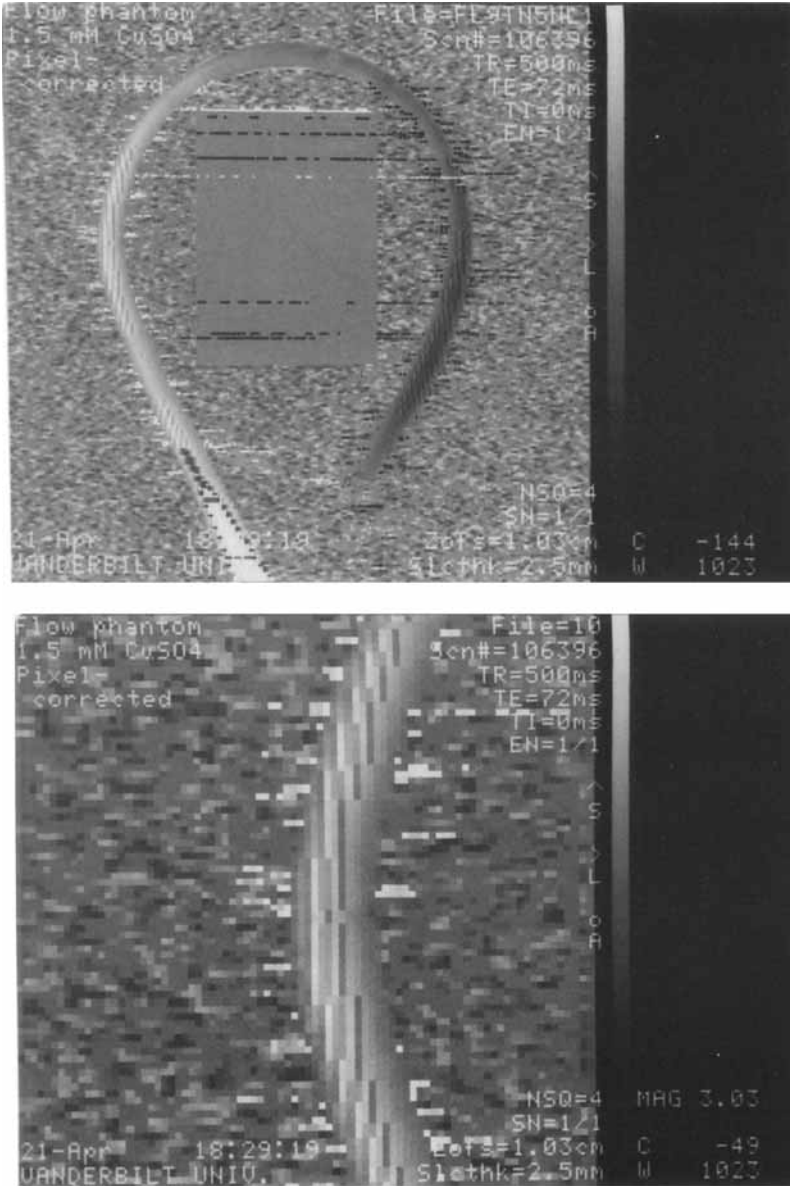
FIG. 3. Corrected phase angle images for a 2.5-mm slice thickness (top), including a magnified image segment (bottom). Correction was by using a search algorithm which reassigned phase angles based on how far the phase has spilled over from the $\pm\pi$ value.

in the voxel, theoretically given by

$$\langle \tan \phi \rangle_{\text{theo}} = \sum_{\substack{\text{voxel} \\ \text{subelements}}} \tan \phi = \sum \frac{I_{\text{im}}}{I_{\text{re}}} = \left\langle \frac{I_{\text{im}}}{I_{\text{re}}} \right\rangle. \qquad [14]$$

The imaged tan ϕ is reconstructed from the volume-averaged real and imaginary components, $\langle I_{re} \rangle$ and $\langle I_{im} \rangle$, according to

$$\langle \tan \phi \rangle_{obs} = \frac{\langle I_{im} \rangle}{\langle I_{re} \rangle} . \qquad [15]$$

When $\phi \approx \pm\pi$, I_{re} does not change much when the phase angle changes in the voxel, so $\langle I_{re} \rangle$ can be used as a least common denominator in Eq. [14]. Also, when $\phi \approx \pm\pi$, the numerator I_{im} is an average of positive and negative values, and is correctly reconstructed (this is not true when components are squared (44)). In this case,

$$\left\langle \frac{I_{im}}{I_{re}} \right\rangle \approx \frac{\langle I_{im} \rangle}{\langle I_{re} \rangle}, \qquad [16a]$$

and

$$\langle \tan \phi \rangle_{obs} \approx \langle \tan \phi \rangle_{theo} \qquad [16b]$$

when $\phi \approx \pm\pi$. Therefore, $\tan(\phi)$ and thus ϕ are correctly volume averaged at the spillover boundary, and the artifacts in Fig. 3 cannot be attributed to volume averaging. The artifacts in Fig. 3 are also not due to noise effects at the phase transition since the errors in phase are systematic and since the noise is predicted to be independent of phase angle.

Instead of being caused by volume averaging, the artifacts at the $-\pi/\pi$ transition are due to the interpolation of 128 phase steps to 256 pixels. Since this interpolation is by sinc convolution of the 128×256 phase angle image, the $-\pi/\pi$ transition is "blunted," producing the artifact in Fig. 3 upon pixel correction. If the interpolation is by zero filling of raw data prior to reconstruction, such an artifact should not occur since the real and imaginary images are continuous at the $-\pi/\pi$ transition.

Dynamic range extension and correction of interpolation artifact using phase reference offsets. Even without interpolation artifacts, the pixel search-and-replace technique can be erratic and introduce artifacts (30). In cases where images are too detailed and vessels are too small to correct on a pixel-by-pixel basis, it is necessary to correct the phase with other methods. In these cases, the spillover can be corrected without artifact by reconstructing multiple images after offsetting the reconstruction reference phase from the true reference phase by 20°, 40°, ... , etc. Thus, pixels which would be in or near a spillover region are placed near the center of the $[-\pi, \pi]$ interval in a region of good phase continuity. For example, the images reconstructed with offsets of 90° and 270° (Fig. 4) have good phase continuity in the regions where the non-offset image (Fig. 1A) has $-\pi/\pi$ transitions. Regions of phase spillover in the non-offset image are then patched with corresponding regions of a phase-offset image having no spillover (after phases in the offset image are reset back to the true reference phase). Phase images corrected in this manner are smooth (Fig. 5) and have provided the basis for production of very accurate images of flow velocity magnitude and direction (45), indicating that the phase reference offset technique accurately reconstructs phase.

Correction of phase spillover using phase reference offsets also extends the dynamic range of phase images since the phase range is extended without changing the phase noise. In this particular study, the measured ratio of phase angle signal range to noise
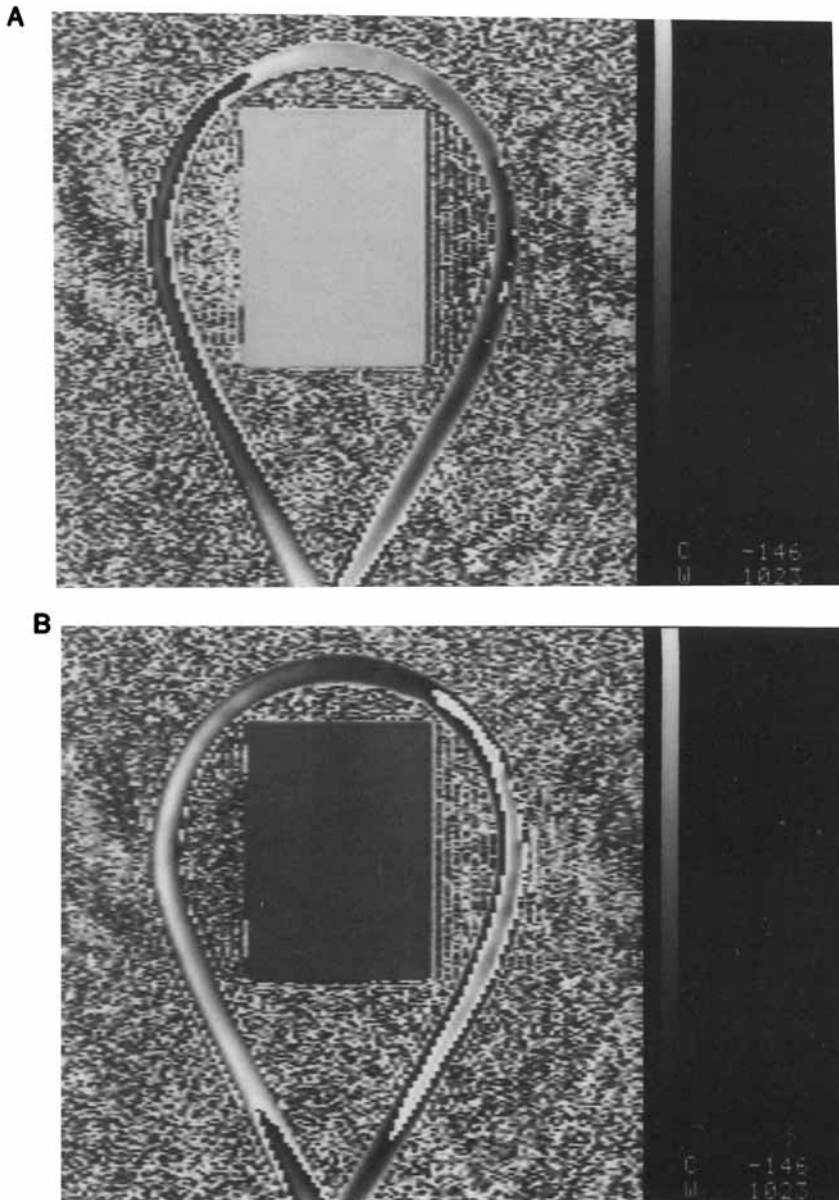
FIG. 4. Phase angle images reconstructed using a correct first-order phase correction and either (a) a zero-order phase correction offset by 90° relative to Fig. 1A, or (B) a zero-order phase correction offset by 270° relative to Fig. 1A.

was improved from 515:1 to 1132:1, compared to the corresponding magnitude-reconstructed value of 75:1, in agreement with theory (see Table 1). Phase correction with multiple phase reference offsets can conceivably be automated for clinical use.
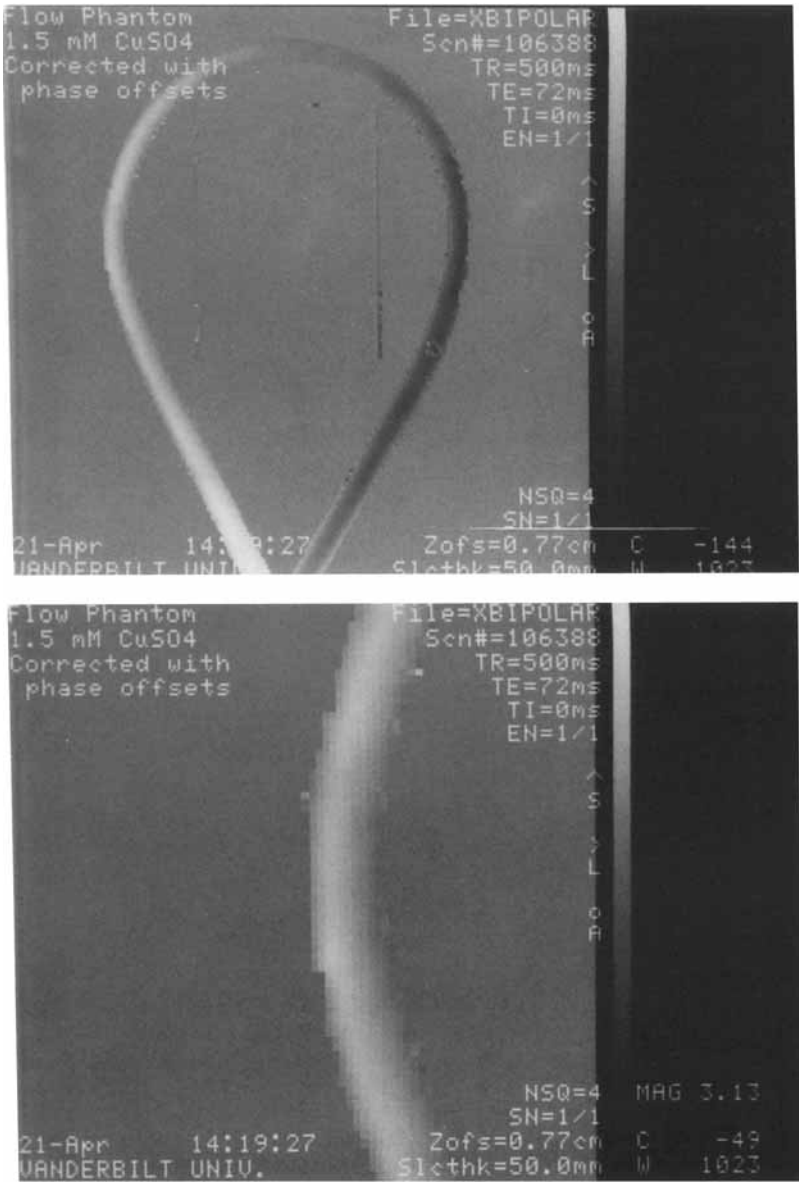
FIG. 5. Phase angle image (top) reconstructed using phase reference offsets, including a magnified image segment (bottom).

Clinical Results

Clinical images of flow in the portal venous system are presented in Fig. 6. Magnitude (Fig. 6a) and phase angle (Fig. 6b) images are reconstructed from the same raw data

collected from the x-bipolar gradient subsequence (see Methods). It is apparent that, compared to magnitude reconstruction, phase angle reconstruction (Fig. 6) produces a higher signal to noise in the vessel.

DISCUSSION AND CONCLUSION

The noise of phase angle images is phase-independent, intuitively expected since the noise in the two channels is uncorrelated. However, computation of phase from Eq. [1] is found to preserve the phase independence of phase angle noise, a result which is not intuitively obvious. Phase angle MR images have inherently better dynamic range than magnitude images reconstructed from the same raw data set, by a factor of 2π. This dynamic range improvement is surprising since ϕ is obtained from the ratio of two noisy signals and so might be expected to be very noisy.

Also, phase angle images have been thought to be of poor quality because of the very high background noise of air (Fig. 1b). However, this high noise only occurs where the magnitude signal is near zero since phase angle noise is inversely proportional to the magnitude signal to noise ratio. On the other hand, image information is contained in regions where signal magnitude is non-zero, in which case the phase angle noise will be relatively low.

The dynamic range advantage results in a signal-to-noise advantage in clinical flow imaging (Fig. 6). If static signal suppression were used in this clinical case, this signal-to-noise improvement would also produce an improvement in contrast-to-noise of vessel minus background tissue. Flow encoding difference techniques which suppress static tissues or quantitate flow velocity by subtracting two images (e.g., rephased minus dephased magnitude, or x-bipolar minus phase-null phase) will also have a maximal 2π-fold signal-to-noise advantage using phase angle reconstructed techniques. These quantitative signal-to-noise predictions should be useful in designing optimal pulse sequences and reconstruction techniques.

The agreement between theory and results verifies that the noise in the two receiver channels is uncorrelated in this particular experimental system, indicating that sample noise has random phase and that instrumental sources of correlated noise, such as the preamplifier and RF transmitter, are less significant. If uncorrelated instrument noise sources were significant, phase angle noise could conceivably be reduced further by designing common channel circuitry to correlate the noise of the two channels.

The dynamic range of phase images is shown to be extended by selecting techniques which cause large phase shifts, followed by correction of the regions of phase spillover by offsetting the reconstruction-based phase reference. This correction also enables unambiguous referencing of parametric data in phase images and avoids artifacts caused by pixel interpolation and pixel searches.

The higher dynamic range of phase angle imaging may enable use of smaller voxels, higher resolution, higher bandwidths, higher A/D conversion rates, thinner slices, and shorter TR intervals, all essential for vascular flow imaging and other applications requiring high spatial and temporal resolution. Useful phase angle information can be extracted even when intensity magnitude images are very noisy, such as in long TE images, multiple echo images, images of spectroscopic components or less sensitive nuclei, and rapid data collection techniques such as reduced phase encoding of small regions (46, 47). For example, in a phase angle image the number of phase-encoding
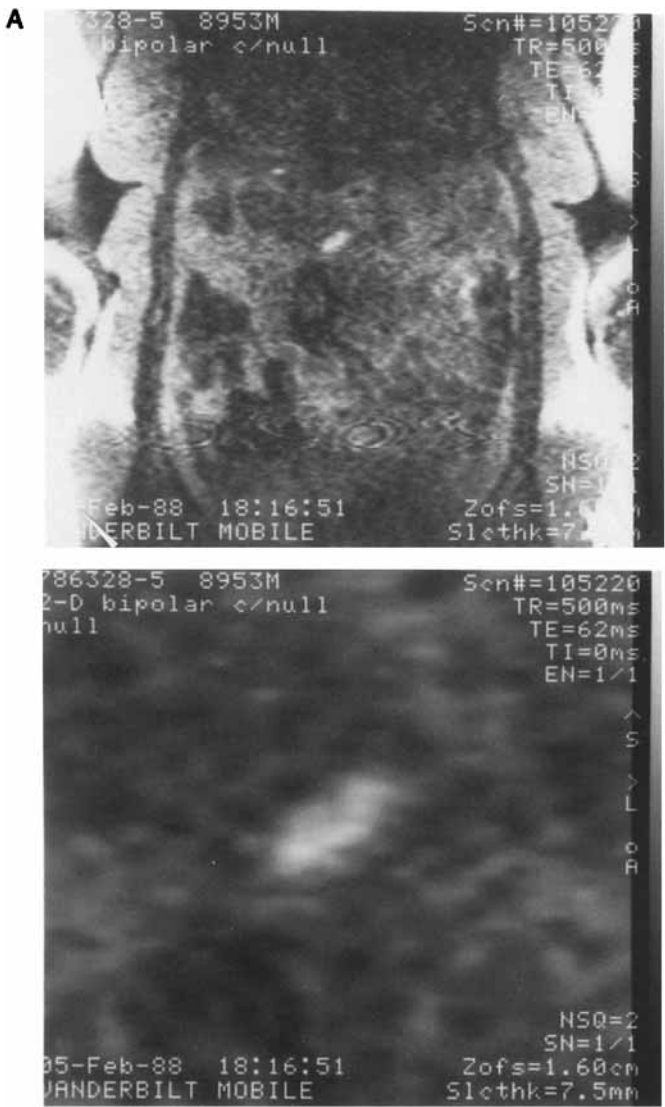
FIG. 6. Magnitude-reconstructed (A) and phase-reconstructed (B) images of flow in the left portal vein (obliquely oriented) and superior mesenteric vein (vertically oriented) including a magnified image segment of the left portal vein (bottom). The images were from the same raw data set acquired with the partially flow-compensated, x-bipolar gradient subsequence (see Methods). The vascular image segment was magnified by cubic-splines pixel interpolation after reconstruction. The center and window of the display were adjusted to span the entire range of grey scale values. Note that the magnitude-reconstructed image is insensitive to flow velocity and so does not have the fine gradations in intensity that the phase angle image has.

steps and the acquisition time can be reduced by a factor of approximately $1/(4\pi^2)$ $\approx 1/40$ to yield the same dynamic range as fully phase-encoded magnitude-reconstructed images. On the other hand, artifacts due to factors such as breathing, which
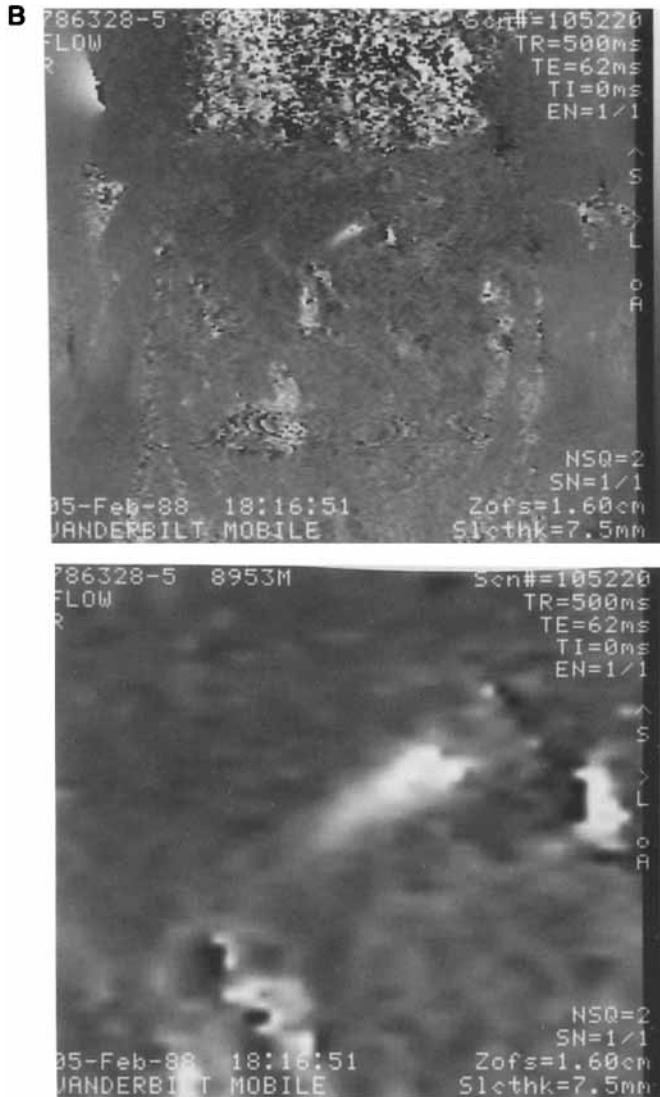
FIG. 6—*Continued*

are of low intensity on magnitude-reconstructed images, will be very prominent on phase angle images due to the low noise of the latter. The high dynamic range suggests that phase imaging may be advantageous over magnitude imaging for studying physical properties such as flow, chemical shift, perfusion, susceptibility, and field inhomogeneity. However, the 2π-fold improvement in signal-to-noise ratio will only be realized if the pulse sequence is appropriately designed so that the physical property of interest can be represented by phases throughout the $[-\pi, \pi]$ interval. It may also be desirable to develop methods to encode other tissue and system properties using the phase angle rather than the signal magnitude.

ACKNOWLEDGMENTS

REFERENCES

1. C. L. DUMOULIN, S. P. SOUZA, AND H. FENG, *Magn. Reson. Med.* **5**, 47 (1987).
2. V. J. WEDEEN, R. A. MEULI, R. R. EDELMAN, S. C. GELLER, L. R. FRANK, T. J. BRADY, AND B. R. ROSEN, *Science* **230**, 946 (1985).
3. V. J. WEDEEN, B. R. ROSEN, R. BUXTON, AND T. J. BRADY, *Magn. Reson. Med.* **3**, 226 (1986).
4. D. G. NISHIMURA, A. MACOVSKI, J. M. PAULY, AND S. M. CONOLLY, *Magn. Reson. Med.* **4**, 193 (1987).
5. D. J. BRYANT, J. A. PAYNE, D. N. FIRMIN, AND D. B. LONGMORE, *J. Comput. Assist. Tomogr.* **8**, 588 (1984).
6. P. R. MORAN, *Magn. Reson. Imaging* **1**, 197 (1982).
7. T. W. REDPATH, D. G. NORRIS, R. A. JONES, AND J. M. S. HUTCHINSON, *Phys. Med. Biol.* **29**, 891 (1984).
8. T. E. CONTURO, R. R. PRICE, A. H. BETH, D. R. PICKENS, C. L. PARTAIN, AND A. E. JAMES, *in* "Soc. of Magn. Reson. in Med., Book of Abstracts," p. 25, New York, NY, 1987.
9. A. HAASE, J. FRAHM, D. MATTHAEI, W. HANICKE, AND K.-D. MERBOLDT, *J. Magn. Reson.* **67**, 258 (1986).
10. I. J. COX, G. M. BYDDER, D. G. GADIAN, I. R. YOUNG, E. PROCTOR, S. R. WILLIAMS, AND I. HART, *J. Magn. Reson.* **70**, 163 (1986).
11. Y. S. KIM, C. W. MUN, AND Z. H. CHO, *Magn. Reson. Med.* **4**, 452 (1987).
12. E. FEIG, *Phys. Med. Biol.* **31**, 1101 (1986).
13. A. A. MAUDSLEY, H. E. SIMON, AND S. K. HILAL, *J. Phys. E: Sci. Instrum.* **17**, 216 (1984).
14. C. H. OH, S. K. HILAL, AND Z. H. CHO, *in* "Soc. of Magn. Reson. in Med., Book of Abstracts," p. 748, San Francisco, CA, 1988.
15. A. P. CRAWLEY AND R. M. HENKELMAN, *Magn. Reson. Med.* **4**, 34 (1987).
16. W. T. DIXON, *Radiology* **153**, 189 (1984).
17. H. W. PARK AND Z. H. CHO, *Magn. Reson. Med.* **3**, 448 (1986).
18. B. R. ROSEN, V. J. WEDEEN, AND T. J. BRADY, *Radiology* **149**, 240 (1983).
19. D. LeBIHAN, E. BRETON, D. LALLEMAND, P. GRENIER, E. CABANIS, AND M. LAVAL-JEANTET, *Radiology* **161**, 401 (1986).
20. I. R. YOUNG AND G. M. BYDDER, *Radiology* **165**(P), 364 (1987) [Abstract].
21. G. M. BYDDER AND I. R. YOUNG, *J. Comput. Assist. Tomogr.* **9**, 659 (1985).
22. I. R. YOUNG, D. R. BAILES, AND G. M. BYDDER, *Magn. Reson. Med.* **2**, 81 (1985).
23. M. R. MITCHELL, T. E. CONTURO, T. J. GRUBER, AND J. P. JONES, *Invest. Radiol.* **19**, 350 (1984).
24. T. E. CONTURO, G. D. SMITH, R. R. PRICE, A. H. BETH, C. L. PARTAIN, AND A. E. JAMES, *in* "Soc. of Magn. Reson. in Med., Book of Abstracts," p. 524, Montreal, 1986.
25. T. E. CONTURO, R. M. KESSLER, AND A. H. BETH, *Magn. Reson. Med.* **15**, 397 (1990).
26. I. R. YOUNG, A. S. HALL, AND G. M. BYDDER, *Magn. Reson. Med.* **5**, 99 (1987).
27. V. J. WEDEEN, B. R. ROSEN, D. CHESLER, AND T. J. BRADY, *J. Comput. Assist. Tomogr.* **9**, 530 (1985).
28. C. H. OH AND Z. H. CHO, *Phys. Med. Biol.* **31**, 1237 (1986).
29. Y. S. KIM, C. W. MUN, K. J. JUNG, AND Z. H. CHO, *Magn. Reson. Med.* **4**, 289 (1987).
30. H. N. YEUNG AND D. W. KORMOS, *Radiology* **159**, 783 (1986).
31. D. I. HOULT AND P. C. LAUTERBUR, *J. Magn. Reson.* **34**, 425 (1979).
32. P. A. BOTTOMLEY AND E. R. ANDREW, *Phys. Med. Biol.* **23**, 630 (1978).
33. H. BARKHUIJSEN, R. DEBEER, W. M. M. J. BOVEE, AND D. VANORMONDT, *J. Magn. Reson.* **61**, 465 (1985).
34. C. MAILER, J. D. F. DANIELSON, AND B. H. ROBINSON, *Rev. Sci. Instrum.* **56**, 1917 (1985).

35. G. N. HOLLAND, *in* "Nuclear Magnetic Resonance (NMR) Imaging" (C. L. Partain, A. E. James, F. D. Rollo, and R. R. Price, Eds.), p. 141, Saunders Co., Philadelphia, PA, 1983.

36. B. H. ROBINSON, H. THOMANN, A. H. BETH, P. FAJER, AND L. R. DALTON, *in* "EPR and Advanced EPR Studies of Biological Systems" (L. R. Dalton, Ed.), p. 133, CRC Press, Inc., Boca Raton, 1985.

37. E. R. MCVEIGH, R. M. HENKELMAN, AND M. J. BRONSKILL, *Med. Phys.* **12**, 586 (1985).

37a. W. A. EDELSTEIN, P. A. BOTTOMLEY, and L. M. PFEIFER, *Med. Phys.* **11**, 180 (1984).

37b. R. M. HENKELMAN, *Med. Phys.* **12**, 232 (1985).

38. W. S. HINSHAW, *J. Appl. Phys.* **47**, 3709 (1976).

39. A. D. BAIN, *J. Magn. Reson.* **56**, 418 (1984).

40. T. E. CONTURO, A. H. BETH, B. H. ROBINSON, C. L. PARTAIN, AND A. E. JAMES, *in* "Soc. of Magn. Reson. in Med., Book of Abstracts," p. 909, New York, NY, 1987.

41. T. E. CONTURO, R. R. PRICE, A. H. BETH, M. R. MITCHELL, C. L. PARTAIN, AND A. E. JAMES, *Phys. Med. Biol.* **31**, 1361 (1986).

42. T. C. FARRAR AND E. D. BECKER, "Pulse and Fourier Transform NMR: Introduction to Theory and Methods," p. 77, Academic Press, New York, 1971.

43. T. E. CONTURO, A. H. BETH, R. R. PRICE, C. L. PARTAIN, AND A. E. JAMES, *in* "Soc. of Magn. Reson. in Med., Book of Abstracts," p. 808, New York, NY, 1987.

44. T. E. CONTURO AND A. H. BETH, *in* "Soc. of Magn. Reson. in Med., Book of Abstracts," p. 1131, Amsterdam, 1989.

45. T. E. CONTURO, A. H. BETH, R. R. PRICE, G. D. SMITH, D. R. PICKENS, C. L. PARTAIN, AND A. E. JAMES, *in* "Soc. of Magn. Reson. in Med., Book of Abstracts," p. 904, San Francisco, 1988.

46. D. A. FEINBERG, J. C. HOENNINGER, L. E. CROOKS, L. KAUFMAN, J. C. WATTS, A. MITSUAKI, AND M. ARAKAWA, *Radiology* **156**, 743 (1985).

47. T. E. CONTURO, R. R. PRICE, AND A. H. BETH, *Magn. Reson. Med.* **6**, 418 (1988).